https://doi.org/10.5194/egusphere-2023-1046
Preprint. Discussion started: 5 June 2023
© Author(s) 2023. CC BY 4.0 License.

Boundary of nighttime ozone chemical equilibrium in the mesopause region: long-term evolution from 20-year satellite observations

Mikhail Yu. Kulikov[1], Mikhail V. Belikovich[1], Aleksey G. Chubarov[1], Svetlana O. Dementyeva[1], and Alexander M. Feigin[1]

[1]A. V. Gaponov-Grekhov Institute of Applied Physics of the Russian Academy of Sciences, 46 Ulyanov Str., 603950 Nizhny Novgorod, Russia

Correspondence to: Mikhail Yu. Kulikov (mikhail_kulikov@mail.ru)

https://doi.org/10.5194/egusphere-2023-1046
Preprint. Discussion started: 5 June 2023
© Author(s) 2023. CC BY 4.0 License.

Abstract. The assumption of nighttime ozone chemical equilibrium (NOCE) is widely used for retrieval of the Ox-HOx components in the mesopause from rocket and satellite measurements. In this work, recently developed analytical criterion of determining the NOCE boundary is applied (1) to study of connection of this boundary with O and H spatiotemporal variability basing on the 3D chemical transport modeling, and (2) to retrieve and analyze the spatiotemporal evolution of the NOCE boundary in 2002-2021 from SABER/TIMED data set. It was revealed, first, that the NOCE boundary well reproduces the transition zone dividing deep and weak diurnal oscillations of O and H at the low and middle latitudes. Second, the NOCE boundary is sensitive to sporadic abrupt changes in the middle atmosphere dynamics, in particular, due to powerful sudden stratospheric warmings leading to events of elevated (up to ~80 km) stratopause, which took place in January-February 2004, 2006, 2009, 2010, 2012, 2013, 2018 and 2019. Third, the space-time evolution of this characteristics expressed via pressure-height contains a clear signal of 11-year solar cycle in the range of 55ºS-55ºN. In particular, average annual the NOCE boundary averaged in this range of latitudes anticorrelates well with $F_{10.7}$ index with the coefficient of -0.96. Moreover, it shows a weak linear trend of 49.2±36.2 m/decade.

1 Introduction

The mesopause (80-100 km) is an interesting region of Earth' atmosphere possessing quite a number of unique phenomena and processes which can be considered as sensitive indicators/predictors of global climate change and anthropogenic influences on atmospheric composition (e.g., (Thomas et al., 1989)). Here, the temperature at middle and high latitudes in the summer reaches its lowest values (down to 100K (Schmidlin, 1992)). The temperatures below 150K lead to water vapour condensation and formation of the highest altitude clouds on Earth, the so-called Polar Mesospheric Clouds or Noctilucent Clouds, consisting primarily of water ice (Thomas, 1991). In opposite, the temperature of winter mesopause is essentially higher, so there is a strong negative temperature gradient between the summer and winter hemispheres. At these altitudes, atmospheric waves with various spatiotemporal scales are observed, in particular, internal gravity waves coming from the lower atmosphere. Destruction of gravity waves leads to strong turbulence that affects the atmospheric circulation and ultimately manifests itself in the mentioned temperature structure of this region.

Many layer phenomena in the mesopause are connected with the photochemistry of the O_x-HO_x components (O, O_3, H, OH, and HO_2). Here, there is a narrow (in height) transition region where photochemistry behavior transforms rapidly from "deep" diurnal oscillations, when the difference between daytime and nighttime values of the O_x-HO_x components can rich several orders of magnitude, to weak photochemical oscillations. As the result, above this region, there takes place O and H

https://doi.org/10.5194/egusphere-2023-1046
Preprint. Discussion started: 5 June 2023
© Author(s) 2023. CC BY 4.0 License.

accumulation and their layers formation manifesting in the appearance of a secondary ozone maximum and airglow layers of OH and O excited states. Thus, O_x-HO_x photochemistry in the mesopause is responsible for the presence of important (first of all, from a practical point of view) indicators observed in the visible and infrared ranges, which are widely used for ground-based and satellite monitoring of climate changes and waves activity. Moreover, O_x-HO_x photochemistry provides the total chemical heating rate of this region, influences the radiative cooling and other useful airglows (for example, by O_2 excited states), involves in the plasma-chemical reactions and formation of the ionosphere layers. The mentioned transformation of O_x-HO_x behavior with height may happens via the nonlinear response of O_x-HO_x photochemistry to the diurnal variations of solar radiation in the form of subharmonic (with periods of 2, 3, 4, and more days) or the chaotic oscillations (e.g., Sonnemann and Fichtelmann, 1997; Feigin et al., 1998). This unique phenomenon was predicted many years ago (e.g., Sonnemann and Fichtelmann, 1987) and investigated theoretically by models with taking into account of different transport processes (e.g., Sonnemann and Feigin, 1999; Sonnemann et al., 1999; Sonnemann and Grygalashvyly, 2005; Kulikov and Feigin, 2005; Kulikov, 2007; Kulikov et al., 2020). It was revealed, in particular, the appearance of nonlinear response is controlled by the vertical eddy diffusion (Sonnemann and Feigin, 1999; Sonnemann et al., 1999), so that 2-day oscillations can only survive at the real diffusion coefficients, but the eddy diffusion in zonal direction leads to the appearance of so-called reaction-diffusion waves in the form of propagating phase fronts of 2-day oscillations (Kulikov and Feigin, 2005; Kulikov et al., 2020). Recently, the satellite data processing found the first evidence that 2-day photochemical oscillations exist in the real mesopause (Kulikov et al., 2021).

While regular remote sensing measurements of most O_x-HO_x components are still limited, the indirect methods based on the physicochemical assumptions are useful tools to monitor these trace gases. In many papers, the O and H distributions were retrieved from the daytime and nighttime rocket and satellite measurements of the ozone and the volume emission rates of OH(ν), $O(^1S)$, and $O_2(a^1\Delta_g)$ (e.g., Good, 1976; Pendleton et al., 1983; McDade et al., 1985; McDade and Llewellyn, 1988; Evans et al., 1988; Thomas, 1990; Llewellyn et al., 1993; Llewellyn and McDade, 1996; Mlynczak et al., 2007, 2013a, 2013b, 2014, 2018; Smith et al., 2010; Xu et al., 2012; Siskind et al., 2008, 2015). The retrieval technique is based on the assumption of the ozone photochemical/chemical equilibrium and physicochemical model of corresponding airglow, which describe the relations between local O and H values and the measurement data.

The daytime photochemical ozone equilibrium is good approximation everywhere in the mesosphere - lower thermosphere (MLT) region (Kulikov et al., 2017) due to ozone photodissociation, whereas the applicability of the assumption of nighttime ozone chemical equilibrium (NOCE) is limited: there is an altitude boundary upper which NOCE is satisfied with accuracy better than 10%. Below this

https://doi.org/10.5194/egusphere-2023-1046
Preprint. Discussion started: 5 June 2023
© Author(s) 2023. CC BY 4.0 License.

boundary, the ozone equilibrium is disturbed essentially and cannot be used. Good (1976) supposed that NOCE is fulfilled above 60 km, whereas other papers apply the NOCE starting from 80 km, independent of latitude and season. However, studies of NOCE within the framework of the 3D chemical-transport models (Belikovich et al., 2018; Kulikov et al., 2018a) revealed that the boundary of NOCE varies within the range of 81–87 km, depending on latitude and season. Due to the practical necessity to determine the local altitude position of this boundary, Kulikov et al. (2018a) presented a simple criterion localizing of the equilibrium boundary using only the data provided by the SABER (Sounding of the Atmosphere using Broadband Emission Radiometry) instrument onboard the TIMED (Thermosphere Ionosphere Mesosphere Energetics and Dynamics). Using this criterion, Kulikov et al. (2019) retrieved annual evolution of the NOCE boundary from the SABER data. It was revealed that the NOCE boundary essentially depends on season and latitude and can rise up to ~ 86 km. Moreover, the analysis of the NOCE boundary in 2003-2005 showed that this characteristic was sensitive to unusual dynamics of stratospheric polar vortex during Arctic winter 2004, which was named as remarkable winter in the 50-year record of meteorological analyses (Manney et al., 2005). Moreover, Belikovich et al. (2018) found by 3D simulation that the excited OH layer well repeats spatiotemporal variability of the NOCE boundary. These results let us to speculate that the NOCE boundary can be considered as important indicator of mesopause' processes.

The main goals of this paper are (1) to investigate the connection of the NOCE boundary according the mentioned criterion with O and H variability with the use of the 3D chemical transport model, and (2) to retrieve and analyze the spatiotemporal evolution of the NOCE boundary in 2002-2021 from SABER/TIMED data set. In the next section, we present the used model. In Section 3, we describe shortly the criterion to determine the NOCE boundary local height and study how this height relates with features O and H distributions from the 3D model. Section 4 explains the methodology of determining the NOCE boundary from satellite data. Section 5 presents the main results obtained from SABER/TIMED data, which are discussed in Section 6.

2 3D model

We use the 3D chemical transport model of the middle atmosphere developed by the Leibniz Institute of Atmospheric Physics (e.g., Sonnemann et al., 1998; Körner and Sonnemann, 2001; Grygalashvyly et al., 2009; Hartogh et al., 2004, 2011). The three-dimensional fields of temperature and winds were adopted by Kulikov et al. (2018b) from the Canadian Middle Atmosphere Model (Scinocca et al., 2008) with an updated frequency of 6 hours. To exclude unrealistic jumps in the evolution of calculated chemical characteristics, a linear smoothing between two subsequent updates of these

https://doi.org/10.5194/egusphere-2023-1046
Preprint. Discussion started: 5 June 2023
© Author(s) 2023. CC BY 4.0 License.

parameters is applied. The model takes into account 3D advective transport and vertical diffusive transport (both, turbulent and molecular). The Walcek-scheme (Walcek, 2000) and the implicit Thomas algorithm (Morton and Mayers, 1994) are used for advective and diffusive transport, respectively. The model grid includes 118 pressure-height levels (from ground to ~135 km), 32 and 64 levels in latitude and longitude, respectively. The chemical part considers 22 constituents (O, $O(^1D)$, O_3, H, OH, HO_2, H_2O_2, H_2O, N, NO, NO_2, NO_3, N_2O, CH_4, CH_2, CH_3, CH_3O_2, CH_3O, CH_2O, CHO, CO, CO_2), 54 two- and three-body reactions, and 15 photo-dissociation reactions. The model uses pre-calculated dependencies of dissociation rates on the altitude and solar zenith angle (Kremp et al., 1999). For the chemistry calculation, we apply the Shimazaki scheme (Shimazaki, 1985) at the integration time of 9 sec.

3 The NOCE criterion

The nighttime ozone chemistry at the mesopause heights is determined mainly by two reactions R1-R2 (e.g., Allen et al., 1984), see Table 1. Thus, ozone equilibrium concentration ($O_3{}^{eq}$) corresponding to the instantaneous balance between production and loss terms is as follows:

$$O_3{}^{eq} = \frac{k_1 \cdot O \cdot O_2 \cdot M}{k_2 \cdot H}, \qquad (1)$$

where M is air concentration, k_{1-2} are the corresponding rate constants of reactions (see Table 1).

As mentioned above, the NOCE criterion was developed in Kulikov et al. (2018a). The main idea is that the local values of O_3 and $O_3{}^{eq}$ are close to each other ($O_3(t) \approx O_3{}^{eq}(t)$), when $\tau_{O_3} \ll \tau_{O_3{}^{eq}}$, where τ_{O_3} is the ozone lifetime and $\tau_{O_3{}^{eq}}$ is the local time scale of $O_3{}^{eq}$:

$$\tau_{O_3} = \frac{1}{k_2 \cdot H}, \qquad (2)$$

$$\tau_{O_3{}^{eq}} \equiv \frac{O_3{}^{eq}}{|dO_3{}^{eq}/dt|} = \frac{O}{H \cdot \left|\frac{d}{dt}\left(\frac{O}{H}\right)\right|}, \qquad (3)$$

As shown in Kulikov et al. (2018a), $\tau_{O_3{}^{eq}}$ can be determined from a simplified photochemical model describing the O_x-HO_x evolution in the mesopause region (Feigin et al., 1998), so the criterion for validity of the NOCE can be written in the form:

$$Cr = \frac{\tau_{O_3}}{\tau_{O_3{}^{eq}}} = 2\frac{k_1 \cdot k_4 \cdot O_2{}^2 \cdot M^2}{k_2}\left(1 - \frac{k_5 + k_6}{k_3}\right) \cdot \frac{1}{k_2 \cdot H \cdot O_3} \ll 1. \qquad (4)$$

where k_i are the corresponding reaction constants from Table 1. Calculations with the global 3D chemistry-transport model of the middle atmosphere showed (Kulikov et al. 2018a) that the criterion $\tau_{O_3}/\tau_{O_3{}^{eq}} \leq 0.1$ well defines the boundary of the area where $|O_3/O_3{}^{eq} - 1| \leq 0.1$.

https://doi.org/10.5194/egusphere-2023-1046
Preprint. Discussion started: 5 June 2023
© Author(s) 2023. CC BY 4.0 License.

Kulikov et al. (2023) presented the theory of chemical equilibrium of a certain trace gas n. Strictly mathematically, the cascade of the sufficient conditions for $n_i(t) \cong n_i^{eq}(t)$ was derived considering its lifetime, equilibrium concentration and time dependences of these characteristics. In case of the nighttime ozone, it was proved that the $\tau_{O_3}/\tau_{O_3{}^{eq}} \ll 1$ is the main condition for NOCE validity and the criterion $\tau_{O_3}/\tau_{O_3{}^{eq}} \leq 0.1$ limits the possible difference between O_3 and $O_3{}^{eq}$ to be no more than ~10%. Moreover, Kulikov et al. (2023) slightly corrected the expression for the criterion (4):

$$\mathrm{Cr} = 2\frac{k_1 \cdot O_2 \cdot M}{k_2}\left(k_4 \cdot M \cdot O_2 \cdot \left(1 - \frac{k_5 + k_6}{k_3}\right) + k_2 \cdot O_3\right) \cdot \frac{1}{k_2 \cdot H \cdot O_3} \leq 0.1. \quad (5)$$

Other important condition for $O_3 \approx O_3{}^{eq}$ at the time moment t is:

$$e^{\int_{t_{bn}}^{t} \tau_{O_3}{}^{-1} dt} \gg 1, \quad (6)$$

where t_{bn} is the time of the beginning of the night. It means the nighttime data measured near the sunset should be excluded from consideration. Kulikov et al. (2023) revealed that, at the solar zenith angle $\chi >$ 95°, the condition (6) is fulfilled in almost all cases.

Figures 1-3 demonstrate model examples of O and H time-height variations above different points in three months. In order to focus our attention on diurnal oscillations, the concentrations are normalized by mean daily values, correspondingly. One can see in all panels of these Figures, first, below 81-87 km, ”deep” diurnal oscillations occur. Due to the shutdown of sources at night and high rates of the main HO_x and O sinks nonlinearly dependent on air concentration (Konovalov and Feigin, 2000), the variables change during each night within a range of several orders of magnitude with low values of times evolution. Above 83-88 km, the situation differs essentially from the previous case. One can see the relatively weak diurnal oscillations. These regimes of O and H behavior are in consistent each other, i.e. deep H diurnal oscillations correspond to the same dynamics in O and so on. There exists a few km thick layer (transition zone) dividing deep and weak oscillations which height position is depended on latitude and season. In particular, summer middle latitude transition is higher than in winter. Figures 1-3 show also the magenta lines pointing the NOCE boundary in accordance to criterion (5) (Cr = 0.1). One can see that the NOCE criterion almost perfectly reproduces the features of transition zone. Thus, our criterion is not only the useful technical characteristic to retrieve O from satellite data, but it points the important dynamical process in O_x-HO_x photochemistry.

4 Boundary of the NOCE from satellite data

We use the version 2.0 of the SABER data product (Level2A) for the simultaneously measured height profiles of temperature (T), O_3 (at 9.6 μm), and total volume emission rates of OH* transitions at

https://doi.org/10.5194/egusphere-2023-1046
Preprint. Discussion started: 5 June 2023
© Author(s) 2023. CC BY 4.0 License.

2.0 (VER) within the 0.0001–0.02 mbar pressure interval (altitudes approximately 75–105 km) in 2002-2021. We consider only nighttime data when the solar zenith angle χ > 95°.

Kulikov et al. (2018a) noted that the term $k_2 \cdot H \cdot O_3$ in the expression for the NOCE criterion can be rewritten in the form depended on measurable characteristics only with the use of the corresponding OH(v) model by Mlynczak et al. (2013a):

$$k_2 \cdot H \cdot O_3 = VER/A(T, M, O), \quad (7)$$

where $A(T, M, O)$ is a function in square brackets of equation (3) in the paper by Mlynczak et al. (2013a) with parameters corrected by Mlynczak et al. (2018):

$$A(T, M, O) = 0.47 \cdot 118.35/(215.05 + 2.5 \cdot 10^{-11} \cdot O_2 + 3.36 \cdot 10^{-13} \cdot e^{220/T} \cdot N_2 + 3 \cdot 10^{-10} \cdot O) + 0.34 \cdot 117.21/(178.06 + 4.8 \cdot 10^{-13} \cdot O_2 + 7 \cdot 10^{-13} \cdot N_2 + 1.5 \cdot 10^{-10} \cdot O) + 0.47 \cdot 117.21/(215.05 + 2.5 \cdot 10^{-11} \cdot O_2 + 3.36 \cdot 10^{-13} \cdot e^{220/T} \cdot N_2 + 3 \cdot 10^{-10} \cdot O) \cdot (20.05 + 4.2 \cdot 10^{-12} \cdot O_2 + 4 \cdot 10^{-13} \cdot N_2)/(178.06 + 4.8 \cdot 10^{-13} \cdot O_2 + 7 \cdot 10^{-13} \cdot N_2 + 1.5 \cdot 10^{-10} \cdot O).$$

This function is the result of combination of the equations of physicochemical OH* balance in the v = 8 and v = 9 states. It depends on the constants of the processes describing sources and sinks on the corresponding levels, in particular, the OH(v) removal in collisions with O_2, N_2 and O. Below 86-87 km, $A(T, M, O) \cong A(T, M, O = 0) \equiv A(T, M)$ because of relativity small O concentrations. Thus, combining Eqs. (5) and (7), the NOCE criterion for SABER data can be recast in the following form:

$$VER \geq VER_{min}(T, M) = 20 \cdot \frac{k_1 \cdot O_2 \cdot M}{k_2} \left(k_4 \cdot O_2 \cdot M \cdot \left(1 - \frac{k_5 + k_6}{k_3}\right) + k_2 \cdot O_3\right) \cdot A(T, M) \quad (8)$$

Due to the strong air concentration-dependence, VER_{min} decreases rapidly with height. In particular, at 105 km, $VER \gg VER_{min}$. At 75 km, the relationship is the inverse. We determine the local position of the NOCE boundary (pressure level p_{eq} and altitude level z_{eq}) according to the criterion (8), where $VER = VER_{min}(T, M)$. We carried out special verification that approximation $A(T, M, O) \cong A(T, M)$ is valid near the NOCE boundary. With the use of annual SABER data, we calculated simultaneous datasets of $A(T, M)$ and $A(T, M, O)$. In second case, we used retrieved O from the same SABER data. The maximum and mean differences between $A(T, M)$ and $A(T, M, O)$ were found to be ~ 2% and ~ 0.1%, respectively.

The total range of latitudes according to the satellite trajectory over a month is ~(83.5°S - 83.5°N). This range was divided into 20 bins and all single values of p_{eq} and z_{eq} falling into one bin during a month were averaged, respectively. For convenience, mean values of p_{eq} were recalculated into pressure-heights (pseudoheights) ${z_{eq}}^{pa}$. The dependence of ${z_{eq}}^{pa}$ on the pressure was taken from Mlynczak et al. (2013a, 2014).

https://doi.org/10.5194/egusphere-2023-1046
Preprint. Discussion started: 5 June 2023
© Author(s) 2023. CC BY 4.0 License.

Kulikov et al. (2023) studied the systematic uncertainty of the retrieved NOCE boundary height. Following the typical analysis presented, for example, in Mlynczak et al. (2013a, 2014), the uncertainty was obtained by calculating the root-sum-square of the individual sensitivity of the retrieved characteristics to the perturbation of O_3, T, rates of reactions, and parameters of the A function. The systematic error of ${z_{eq}}^{pa}$ and z_{eq} varies in the range of 0.1-0.3 km, whereas the random error is negligible due to averaging in time and space.

5 NOCE boundary in 2002-2021 from SABER/TIMED data: main results

Figures 4-7 demonstrate the contour map of space-time evolution of pseudoheight ${z_{eq}}^{pa}$ in 2002-2021 and examples of ${z_{eq}}^{pa}$ time evolution, mean annual cycle and Fourier spectra at different latitudes. It can be seen, first, above ~55ºS,N, there are data gaps due to the satellite sensing geometry. For example, at 66.8-75.15°S,N in 2002-2014, measurements cover 6 months per year only. In 2015, because of slight change in satellite geometry, additional months appeared. This is especially noticeable above ~66ºS,N and manifests itself by extension of the variation range of ${z_{eq}}^{pa}$ at these latitudes in 2015-2021. Second, the variation range of ${z_{eq}}^{pa}$, annual cycle and spectrum of harmonic oscillations depend essentially on latitude. Near the equator, ${z_{eq}}^{pa}$ varies in the 81-83 km range mainly and there are two main harmonics with periods of 1/2 and 1 year in the spectrum. At low latitudes, the variation range of ${z_{eq}}^{pa}$ narrows down to a minimum (~82.2-83.2 km at 16.7-20.05°S,N) that is accompanied by appearance of wide spectrum of harmonics with periods of 1/5, 1/4, 1/3, 1/2, and 1 year. At middle latitudes, the range of ${z_{eq}}^{pa}$ variation monotonically increases up to ~81-85.5 km with latitude and the harmonic with period of 1 year becomes the main mode in the spectrum of oscillations. At both, low and middle latitudes, there is no signal from quasi-biennial oscillations but one can see remarkable amplitude of harmonic with a period of ~10 years, which can be associated with manifestation of 11-year solar cycle. Note mentioned features are typical for both hemispheres. At high latitudes, ${z_{eq}}^{pa}$ varies in the range of 79-86 km. At these latitudes, it can seen the main difference between north and south hemispheres: the sharp falls and rises of the north boundary of NOCE by several km (up to 3-4 km) appearing in January-February 2004, 2006, 2009, 2010, 2012, 2013, 2018 and 2019 and absenting at south latitudes.

Analyzing the Figure 6, one can note the following redistribution in the annual cycle with increasing latitude from equator to polar latitudes. Near the equator, the annual cycle has two maxima in June – July and in December – January. The first one is more pronounced. That is why there are two main harmonics with periods of 1/2 and 1 year in the spectrum. At low latitudes, one maximum (summer)

© Author(s) 2023. CC BY 4.0 License.

remains in place, and the other begins to approach the first. As the result, the wide spectrum of harmonics takes place. At middle latitudes, the maxima gradually merge so that the 1 year-harmonic becomes the main.

Figures 8-9 demonstrate the contour map of space-time evolution of average annual ${z_{eq}}^{pa}$ ($< {z_{eq}}^{pa} >$, hereafter, the angle brackets are used to denote the values averaged in time and space) in 2002-2021 and examples of time evolution of this characteristic at different latitudes. Basing on Fourier' spectra presented in Figure 7, we can suppose that, at low and middle latitudes, the interannual variation of $< {z_{eq}}^{pa} >$ is caused by 11-year solar cycle mainly. Figure 10 presents the correlation coefficient of $< {z_{eq}}^{pa} >$ with $F_{10.7}$ index (solar radio flux at 10.7 cm, see red curve in Figure 8) as a function of latitude. One can see good anticorrelation (with coefficient from -0.74 to -0.9) between ~55ºS and ~55ºN. At high latitudes, the absolute value of correlation coefficient decreases sharply up to 0.56 in the south and 0.1 in the north. Blue curve in Figure 11 shows latitude-averaged $< {z_{eq}}^{pa} >$ in the range of 55ºS-55ºN. In this case, the anticorrelation with $F_{10.7}$ index is close to ideal (coefficient ~ -0.96).

With the use of multiple linear regression:

$$< {z_{eq}}^{pa} > (year) = const + \alpha \cdot year + \beta \cdot F_{10.7}(year), \quad (9)$$

we determined slow linear trend in $< {z_{eq}}^{pa} >$ as a function of latitude in the range of 55ºS-55ºN (see Figure 12). One can see a tendency to increase $< {z_{eq}}^{pa} >$ at most latitudes with trend up to 10 m/year, but with high uncertainty. Applying the regression analysis to latitude-averaged $< {z_{eq}}^{pa} >$ (blue curve in Figure 11) gives us a more statistically significant value of the trend: 4.92±3.62 m/year.

Figures 13-16 demonstrate the contour map of space-time evolution of real altitude of NOCE boundary in 2002-2021, examples of z_{eq} time evolution, mean annual cycle and the Fourier spectra at different latitudes. Comparing with Figures 4-7, it can be seen, first, z_{eq} repeats many qualitative features of space-time evolution of ${z_{eq}}^{pa}$. In particular, in the direction from the equator to the poles, the variation range of z_{eq} first decreases up to 1 km at 16º-25ºS,N, then expanding to several km at middle and high latitudes. In Figure 15, one can see the same redistribution of the annual cycle with latitude, as it was mentioned in Figure 6. Near the equator, the annual cycle possesses two maxima occurring in June – July and in December – January. At low latitudes, one maximum continues to be in summer, whereas the other shifts into the spring. At middle latitudes, the maxima gradually coalesce forming a single summer maximum. At north high latitudes, there are the same local sharp variations of the NOCE boundary in January-February 2004, 2006, 2009, 2010, 2012, 2013, 2018 and 2019, which absent at south latitudes. Second, on average, z_{eq} is lower than ${z_{eq}}^{pa}$. The difference ${z_{eq}}^{pa} - z_{eq}$ varies in the range of 0 - 1.5 km

https://doi.org/10.5194/egusphere-2023-1046
Preprint. Discussion started: 5 June 2023
© Author(s) 2023. CC BY 4.0 License.

at equator, 0 – 2.5 km at 50º-58ºS,N and 1-4 km at 75º-83ºS,N. The maxima and minima of ${z_{eq}}^{pa} - z_{eq}$ are reached in winter and summer, respectively. In general, the variation range of z_{eq} during the year is wider by about 1.5-4 km depending on latitude. Third, the spectra of harmonic oscillations are similar to ${z_{eq}}^{pa}$ spectra except for no signal of the 11-year solar cycle.

Figures 17-18 demonstrate the contour map of space-time evolution of average annual z_{eq} ($< z_{eq} >$) in 2002-2021 and examples of time evolution of this characteristics at different latitudes. One can see, at all latitudes, there is no clear evidence of 11-year solar cycle manifestation. This is confirmed by the calculation of the correlation coefficient of $< z_{eq} >$ with $F_{10.7}$ index as a function of latitude (see Figure 19). Moreover, the latitude-averaged (in the range of 55ºS-55ºN) $< z_{eq} >$ has a correlation coefficient equal to -0.54.

With the use of multiple linear regression as in the case of $< {z_{eq}}^{pa} >$, we determined slow linear trend in $< z_{eq} >$ as a function of latitude in the range of 55ºS-55ºN (see Figure 20). One can see a tendency to decrease $< z_{eq} >$ at most latitudes with trend up to -10 m/year, but with high uncertainty. Applying the regression analysis to latitude-averaged $< z_{eq} >$ gives us the trend equal to -4.48±6.73 m/year.

6 Discussion

The NOCE boundary is important technical characteristics for the correct application of NOCE approximation to retrieve the nighttime distributions of minor chemical species of MLT. Remind also, that Belikovich et al. (2018) found by 3D simulation that the excited hydroxyl layer well repeats spatiotemporal variability of the NOCE boundary. Let discus the obtained results from the point of view of other possible applications of this feature.

The carried out analysis revealed unusual behavior of the NOCE boundary at the north pole latitudes in January-February 2004, 2006, 2009, 2010, 2012, 2013, 2018 and 2019. All these time periods are known for strong local changes of the middle atmosphere dynamics due to extremely powerful sudden stratospheric warming which leaded to appearance of elevated (from typical 50-60 km to ~80 km) stratopause events (see García-Comas et al. (2020) and references there). Thus, we can speculate that the boundary of NOCE is sensitive to sporadic abrupt changes in the dynamics of the middle atmosphere.

The space-time evolution of the NOCE boundary expressed in terms of pseudoheights contains a clear signal of the 11-year solar cycle in the range of 55ºS-55ºN, which is suppressed mainly at high

https://doi.org/10.5194/egusphere-2023-1046
Preprint. Discussion started: 5 June 2023
© Author(s) 2023. CC BY 4.0 License.

latitudes. The weak correlation of ${z_{eq}}^{pa}$ with $F_{10.7}$ index at south high latitudes may be caused by the mentioned data gaps due to satellite sensing geometry. The same reason and distortions by sudden stratospheric warming, evidently, determine no correlation at north high latitudes. Thus, ${z_{eq}}^{pa}$ at low and middle latitudes can be considered as sensitive indicator of solar activity. The analysis of reasons why solar cycle does not manifest itself in spatio-temporal variability of z_{eq} requires a separate study and is beyond the scope of this work.

Figures 6 and 15 present interesting peculiarity. At middle latitudes, summer ${z_{eq}}^{pa}$ and z_{eq} are remarkably (for several kilometers) higher than winter ones, while the opposite relationship could be expected. Due to more effective daytime HO_x photoproduction at these altitudes, summer H values at the beginning of nights are higher than the ones in winter. So, the summer ozone lifetimes should be less and condition of NOCE is more favorable than in winter. Nevertheless, the same ratio between summer and winter the NOCE boundaries at middle latitudes was revealed in Belikovich et al. (2018) and Kulikov et al. (2018a), where the boundary of this equilibrium was determined by direct comparison of O_3 and ${O_3}^{eq}$ concentrations from results of 3-D chemical-transport models. Based on results in Section 3, one can assume that the discussed effect is connected with the height position of the transition zone, which demonstrates the same variation (see Figures 1-3). Kulikov et al. (2023) derived the equations describing pure chemical O and H nighttime evolution:

$$\begin{cases} \frac{dO}{dt} = -2 \cdot k_4 \cdot M \cdot O_2 \cdot H - 2 \cdot k_2 \cdot H \cdot O_3 \\ \frac{dH}{dt} = -2 \cdot k_4 \cdot M \cdot O_2 \cdot \frac{k_5+k_6}{k_3} \cdot \frac{H^2}{O} \end{cases} . \quad (10)$$

Neglecting the second term in the first equation as secondary, this system can be analytically solved, so that nighttime evolution times of O and H are as follows:

$$\tau_O \equiv \frac{O}{|dO/dt|} = \frac{1}{2 \cdot k_4 \cdot M \cdot O_2} \cdot \left(\frac{O}{H}\right)_{t=t_{bn}} - \left(1 - \frac{k_5+k_6}{k_3}\right) \cdot (t - t_{bn}), \quad (11)$$

$$\tau_H \equiv \frac{H}{|dH/dt|} = \frac{1}{2 \cdot k_4 \cdot M \cdot O_2} \cdot \frac{k_3}{k_5+k_6} \cdot \left(\frac{O}{H}\right)_{t=t_{bn}} - \left(\frac{k_3}{k_5+k_6} - 1\right) \cdot (t - t_{bn}), \quad (12)$$

where t_{bn} is the time of the beginning of the night, $\left(\frac{O}{H}\right)_{t=t_{bn}}$ is the ratio O/H at the beginning of the night. Note that k_3 is essentially larger than $k_5 + k_6$ (see Table 1). Basing on daytime O and H distributions in mesopause region obtained in Kulikov et al. (2022), we calculated O/H in summer and winter. During the summer, this ratio at middle latitudes is remarkably less than in winter, whereas air concentration increases due to a decrease in temperature. As the result, summer τ_O and τ_H are essentially less their winter values that explain the summer rise of transition zone and the NOCE boundary.

https://doi.org/10.5194/egusphere-2023-1046
Preprint. Discussion started: 5 June 2023
© Author(s) 2023. CC BY 4.0 License.

7 Conclusions

The NOCE criterion is not only the useful technical characteristics to retrieve O from satellite data, but it reproduces the transition zone position, which divides deep and weak diurnal oscillations of O and H at low and middle latitudes.

The boundary of NOCE according the criterion is sensitive to sporadic abrupt changes in the dynamics of the middle atmosphere.

The NOCE boundary at low and middle latitudes expressed in pseudoheight contains a clear signal of 11-year solar cycle and can be considered as sensitive indicator of solar activity.

At middle latitudes, summer boundary of NOCE is remarkably (for several kilometers) higher than winter one that is accompanied by the same variation of the transition zone. This effect is explained by the markedly lower values of the O and H nighttime evolution times in summer than in winter due to lower values of the ratio O/H at the beginning of the night and air concentration increase.

Data availability. The SABER data are obtained from the website (https://saber.gats-inc.com). The data of solar radio flux at 10.7 cm in 2002-2021 were downloaded from http://www.wdcb.ru/stp/solar/solar_flux.ru.html and https://www.spaceweather.gc.ca/forecast-prevision/solar-solaire/solarflux/sx-5-en.php.

Code availability. Code is available upon request.

Author contributions. MK and MB carried out the data processing and analysis and wrote the manuscript. AC, SD, and AM contributed to reviewing the article.

Competing interests. The authors declare that they have no conflict of interest.

Acknowledgements. The authors are grateful to the SABER team for data availability.

Financial support. This work was supported by the Russian Science Foundation under grant No. 22-12-00064 (https://rscf.ru/project/22-12-00064/) and state assignment no. 0729-2020-0037.

https://doi.org/10.5194/egusphere-2023-1046
Preprint. Discussion started: 5 June 2023
© Author(s) 2023. CC BY 4.0 License.

References

Allen, M., Lunine, J. I., and Yung, Y. L. The vertical distribution of ozone in the mesosphere and lower thermosphere, J. Geophys. Res., 89(D3), 4841–4872, https://doi.org/10.1029/JD089iD03p04841, 1984.

Belikovich, M. V., Kulikov, M. Yu, Grygalashvyly, M., Sonnemann, G. R., Ermakova, T. S., Nechaev, A. A., and Feigin, A .M.: Ozone chemical equilibrium in the extended mesopause under the nighttime conditions, Adv. Space Res., 61, 426–432, https://doi.org/10.1016/j.asr.2017.10.010, 2018.

Burkholder, J. B., Sander, S. P., Abbatt, J., Barker, J. R., Cappa, C., Crounse, J. D., Dibble, T. S., Huie, R. E., Kolb, C. E., Kurylo, M. J., Orkin, V. L., Percival, C. J., Wilmouth, D. M., and Wine, P. H.: Chemical Kinetics and Photochemical Data for Use in Atmospheric Studies, Evaluation No. 19, JPL Publication 19-5, Jet Propulsion Laboratory, Pasadena, http://jpldataeval.jpl.nasa.gov, 2020.

Evans, W. F. J., McDade, I. C., Yuen, J., and Llewellyn, E. J.: A rocket measurement of the O_2 infrared atmospheric (0-0) band emission in the dayglow and a determination of the mesospheric ozone and atomic oxygen densities, Can. J. Phys., 66, 941–946, https://doi.org/10.1139/p88-151. 1988.

García-Comas, M., Funke, B., López-Puertas, M., González-Galindo, F., Kiefer, M., and Höpfner, M.: First detection of a brief mesoscale elevated stratopause in very early winter. Geophys. Res. Lett., 47, e2019GL086751, https://doi.org/10.1029/2019GL086751, 2020.

Good, R. E.: Determination of atomic oxygen density from rocket borne measurements of hydroxyl airglow, Planet. Space Sci., 24, 389–395, https://doi.org/10.1016/0032-0633(76)90052-0, 1976.

Grygalashvyly, M., Sonnemann, G. R., and Hartogh, P.: Long-term behavior of the concentration of the minor constituents in the mesosphere - A model study, Atmos. Chem. Phys., 9, 2779–2792, https://doi.org/10.5194/acp-9-2779-2009, 2009.

Hartogh, P., Jarchow, C., Sonnemann, G. R., and Grygalashvyly, M.: On the spatiotemporal behavior of ozone within the upper mesosphere/mesopause region under nearly polar night conditions, J. Geophys. Res., 109, D18303, https://doi.org/10.1029/2004JD004576, 2004.

Hartogh, P., Jarchow, Ch., Sonnemann, G. R., and Grygalashvyly, M.: Ozone distribution in the middle latitude mesosphere as derived from microwave measurements at Lindau (51.66°N, 10.13°E), J. Geophys. Res., 116, D04305, https://doi.org/10.1029/2010JD014393, 2011.

Feigin, A. M., Konovalov, I. B., and Molkov, Y. I.: Towards understanding nonlinear nature of atmospheric photochemistry: Essential dynamic model of the mesospheric photochemical system., J. Geophys. Res.: Atmos., 103, 25,447–25,460, https://doi.org/10.1029/98JD01569, 1998.

Konovalov, I. B., and Feigin, A. M.: Towards an understanding of the non-linear nature of atmospheric photochemistry: origin of the complicated dynamic behavior of the mesospheric photochemical system, Nonlin. Processes Geophys., 87-104, https://doi.org/10.5194/npg-7-87-2000, 2000.

https://doi.org/10.5194/egusphere-2023-1046
Preprint. Discussion started: 5 June 2023
© Author(s) 2023. CC BY 4.0 License.

Körner, U., and Sonnemann, G. R.: Global 3D-modeling of water vapor concentration of the mesosphere/mesopause region and implications with respect to the NLC region, J. Geophys. Res., 106, 9639– 9651, https://doi.org/10.1029/2000JD900744, 2001.

Kremp, C., Berger, U., Hoffmann, P., Keuer, D., and Sonnemann, G. R.: Seasonal variation of middle latitude wind fields of the mesopause region—A comparison between observation and model calculation, Geophys. Res. Lett., 26, 1279–1282, https://doi.org/10.1029/1999GL900218, 1999.

Kulikov, M. Yu., and Feigin, A. M.: Reactive-diffusion waves in the mesospheric photochemical system. Adv. Space Res., 35(11), 1992-1998, https://doi.org/10.1016/j.asr.2005.04.020, 2005.

Kulikov, M. Yu.: Theoretical investigation of the influence of a quasi 2-day wave on nonlinear photochemical oscillations in the mesopause region, J. Geophys. Res., 112, D02305, https://doi.org/10.1029/2005JD006845, 2007.

Kulikov, M. Y., Belikovich, M. V., Grygalashvyly, M., Sonnemann, G. R., Ermakova, T. S., Nechaev, A. A., and Feigin, A. M.: Daytime ozone loss term in the mesopause region, Ann. Geophys., 35, 677-682 https://doi.org/10.5194/angeo-35-677-2017, 2017.

Kulikov, M. Y., Belikovich, M. V., Grygalashvyly, M., Sonnemann, G. R., Ermakova, T. S., Nechaev, A. A., and Feigin, A. M.: Nighttime ozone chemical equilibrium in the mesopause region. J. Geophys. Res.,123, 3228–3242, https://doi.org/10.1002/2017JD026717, 2018a.

Kulikov, M. Y., Nechaev, A. A., Belikovich, M. V., Ermakova, T. S., and Feigin, A. M.: Technical note: Evaluation of the simultaneous measurements of mesospheric OH, HO_2, and O_3 under a photochemical equilibrium assumption – a statistical approach, Atm. Chem. Phys., 18, 7453-747, https://doi.org/10.5194/acp-18-7453-2018, 2018b.

Kulikov, M. Yu., Nechaev, A. A., Belikovich, M. V., Vorobeva, E. V., Grygalashvyly, M., Sonnemann, G. R., and Feigin, A. M.: Border of nighttime ozone chemical equilibrium in the mesopause region from saber data: implications for derivation of atomic oxygen and atomic hydrogen, Geophys. Res. Lett., 46, 997– 1004, https://doi.org/10.1029/2018GL080364, 2019.

Kulikov, M. Y., Belikovich, M. V., and Feigin, A. M.: Analytical investigation of the reaction-diffusion waves in the mesopause photochemistry, J. Geophys. Res., 125, e2020JD033480, https://doi.org/10.1029/2020JD033480, 2020.

Kulikov, M. Y., Belikovich, M. V., Feigin, A. M.: The 2-day photochemical oscillations in the mesopause region: the first experimental evidence? Geophys. Res. Lett., 48, e2021GL092795, https://doi.org/10.1029/2021GL092795, 2021.

Kulikov, M. Y., Belikovich, M. V., Grygalashvyly, M., Sonnemann, G. R., and Feigin, A.M.: The revised method for retrieving daytime distributions of atomic oxygen and odd-hydrogens in the mesopause region from satellite observations, Earth Planets Space, 74, 44, https://doi.org/10.1186/s40623-022-01603-8, 2022.

https://doi.org/10.5194/egusphere-2023-1046
Preprint. Discussion started: 5 June 2023
© Author(s) 2023. CC BY 4.0 License.

Kulikov, M. Yu., Belikovich, M. V., Chubarov, A. G., Dementeyva, S. O., Feigin, A. M.: Boundary of nighttime ozone chemical equilibrium in the mesopause region: improved criterion of determining the boundary from satellite data, Adv. Space Res., 71 (6), 2770-2780, https://doi.org/10.1016/j.asr.2022.11.005, 2023.

Llewellyn, E. J., McDade, I. C. Moorhouse, P. and Lockerbie M. D.: Possible reference models for atomic oxygen in the terrestrial atmosphere, Adv. Space Res., 13, 135–144, https://doi.org/10.1016/0273-1177(93)90013-2, 1993.

Llewellyn, E. J., and McDade, I. C.: A reference model for atomic oxygen in the terrestrial atmosphere, Adv. Space Res., 18, 209–226, https://doi.org/10.1016/0273-1177(96)00059-2, 1996.

Manney, G. L., Kruger, K., Sabutis, J. L., Sena, S. A., and Pawson, S.: The remarkable 2003–2004 winter and other recent warm winters in the Arctic stratosphere since the late 1990s. J. Geophys. Res., 110, D04107, https://doi.org/10.1029/2004JD005367, 2005.

McDade, I. C., Llewellyn, E. J., and Harris, F. R.: Atomic oxygen concentrations in the lower auroral thermosphere, Adv. Space Res., 5, 229–232, https://doi.org/10.1029/GL011I003P00247, 1985.

McDade, I. C., and Llewellyn, E. J.: Mesospheric oxygen atom densities inferred from night-time OH Meinel band emission rates, Planet. Space Sci., 36, 897–905, https://doi.org/10.1016/0032-0633(88)90097-9, 1988.

Mlynczak, M. G., Marshall, B. T., Martin-Torres, F. J., Russell III, J. M., Thompson, R. E., Remsberg, E. E., and Gordley, L. L.: Sounding of the Atmosphere using Broadband Emission Radiometry observations of daytime mesospheric $O_2(^1D)$ 1.27 µm emission and derivation of ozone, atomic oxygen, and solar and chemical energy deposition rates, J. Geophys. Res., 112, D15306, https://doi.org/10.1029/2006JD008355, 2007.

Mlynczak, M. G., Hunt, L. A., Mast, J. C., Marshall, B. T., Russell III, J. M., Smith, A. K., Siskind, D. E., Yee, J.-H., Mertens, C. J., Martin-Torres, F. J., Thompson, R. E., Drob, D. P., and Gordley, L. L.: Atomic oxygen in the mesosphere and lower thermosphere derived from SABER: Algorithm theoretical basis and measurement uncertainty, J. Geophys. Res., 118, 5724–5735, https://doi.org/10.1002/jgrd.50401, 2013a.

Mlynczak, M. G., Hunt, L. H., Mertens, C. J., Marshall, B. T., Russell III, J. M., López-Puertas, M., Smith, A. K., Siskind, D. E., Mast, J. C., Thompson, R. E., and Gordley, L. L.: Radiative and energetic constraints on the global annual mean atomic oxygen concentration in the mesopause region, J. Geophys. Res. Atmos., 118, 5796–5802, https://doi.org/10.1002/jgrd.50400, 2013b.

Mlynczak, M. G., Hunt, L. A. Marshall, B. T. Mertens, C. J. Marsh, D. R. Smith, A. K. Russell, J. M. Siskind D. E., and Gordley L. L.: Atomic hydrogen in the mesopause region derived from SABER: Algorithm theoretical basis, measurement uncertainty, and results, J. Geophys. Res., 119, 3516–3526, https://doi.org/10.1002/2013JD021263, 2014.

https://doi.org/10.5194/egusphere-2023-1046
Preprint. Discussion started: 5 June 2023
© Author(s) 2023. CC BY 4.0 License.

Mlynczak, M. G., Hunt, L. A., Russell, J. M. III, and Marshall, B. T.: Updated SABER night atomic oxygen and implications for SABER ozone and atomic hydrogen, Geophys. Res. Lett., 45, 5735–5741, https://doi.org/10.1029/2018GL077377, 2018.

Morton, K. W., and Mayers, D. F.; Numerical Solution of Partial Differential Equations, Cambridge University Press, 1994.

Pendleton, W. R., Baker, K. D., Howlett, L. C.: Rocket-based investigations of O(^{3}P), O_2 ($a^1\Delta_g$) and OH* (v=1,2) during the solar eclipse of 26 February 1979, J. Atm. Terr. Phys., 45(7), 479-491, 1983.

Siskind, D. E., Marsh, D. R., Mlynczak, M. G., Martin-Torres, F. J., and Russell III, J. M.: Decreases in atomic hydrogen over the summer pole: Evidence for dehydration from polar mesospheric clouds? Geophys. Res. Lett., 35, L13809, https://doi.org/10.1029/2008GL033742, 2008.

Siskind, D. E., Mlynczak, M. G., Marshall, T., Friedrich, M., Gumbel, J.: Implications of odd oxygen observations by the TIMED/SABER instrument for lower D region ionospheric modeling, J. Atmos. Sol. Terr. Phys., 124, 63–70, https://doi.org/10.1016/j.jastp.2015.01.014, 2015.

Schmidlin, F .J.: First observation of mesopause temperature lower than 100 K, Geophys. Res. Lett., 19, 1643-1646, https://doi.org/10.1029/92GL01506, 1992.

Shimazaki, T.: Minor Constituents in the Middle Atmosphere, D. Reidel, Norwell, Mass., USA, 444 pp., 1985.

Smith, A. K., Marsh, D. R. Mlynczak, M. G. and Mast J. C.: Temporal variations of atomic oxygen in the upper mesosphere from SABER, J. Geophys. Res., 115, D18309, https://doi.org/10.1029/2009JD013434, 2010.

Sonnemann, G., and Fichtelmann, B.: Enforced oscillations and resonances due to internal non-linear processes of photochemical system in the atmosphere, Acta. Geod. Geophys. Mont. Hung., 22, 301–311, 1987.

Sonnemann, G., and Fichtelmann, B.: Subharmonics, cascades of period of doubling and chaotic behavior of photochemistry of the mesopause region, J. Geophys. Res., 101, 1193-1203, https://doi.org/10.1029/96JD02740, 1997.

Sonnemann, G., Kremp, C. Ebel, A. and Berger U.: A three-dimensional dynamic model of minor constituents of the mesosphere, Atmos. Environ., 32, 3157–3172, https://doi.org/10.1016/S1352-2310(98)00113-7, 1998.

Sonnemann, G., Feigin, A. M., and Molkov, Ya. I.: On the influence of diffusion upon the nonlinear behaviour of the photochemistry of the mesopause region, J. Geophys. Res., 104, 30591-30603, https://doi.org/10.1029/1999JD900785, 1999.

Sonnemann, G., and Feigin, A. M.: Non-linear behaviour of a reaction-diffusion system of the photochemistry within the mesopause region, Phys. Rev. E, 59, 1719-1726, https://doi.org/10.1103/PhysRevE.59.1719, 1999.

https://doi.org/10.5194/egusphere-2023-1046
Preprint. Discussion started: 5 June 2023
© Author(s) 2023. CC BY 4.0 License.

Sonnemann, G. R.: The photochemical effects of dynamically induced variations in solar insolation, J. Atmos. Sol. Terr. Phys., 63, 781-797, https://doi.org/10.1016/S1364-6826(01)00010-4, 2001.

Sonnemann, G. R., and Grygalashvyly, M.: On the two-day oscillations and the day-to-day variability in global 3-D-modeling of the chemical system of the upper mesosphere/mesopause region, Nonlin. Processes Geophys., 12, 691– 705, https://doi.org/10.5194/npg-12-691-2005, 2005.

Thomas, G. E., Olivero, J. J., Jensen, E. J., Schroder, W., and Toon, O. B.: Relation between increasing methane and the presence of ice clouds at the mesopause, Nature, 338, 490–492https://doi.org/10.1038/338490a0, 1989.

Thomas, R. J.: Atomic hydrogen and atomic oxygen density in the mesosphere region: Global and seasonal variations deduced from Solar Mesosphere Explorer near-infrared emissions, J. Geophys. Res., 95, 16,457–16,476, https:// doi. org/ 10. 1029/ JD095 iD10p 16457, 1990.

Thomas, G. E.: Mesospheric clouds and the physics of the mesopause region, Rev. Geophys., 29, 553–575, https://doi.org/10.1029/91RG01604, 1991.

Walcek, C. J.: Minor flux adjustment near mixing ratio extremes for simplified yet highly accurate monotonic calculation of tracer advection, J. Geophys. Res., 105, 9335-9348, https://doi.org/10.1029/1999JD901142, 2000.

Xu, J., Gao, H. Smith, A. K. and Zhu Y.: Using TIMED/SABER nightglow observations to investigate hydroxyl emission mechanisms in the mesopause region, J. Geophys. Res., 117, D02301, https://doi.org/10.1029/2011JD016342, 2012.

https://doi.org/10.5194/egusphere-2023-1046
Preprint. Discussion started: 5 June 2023
© Author(s) 2023. CC BY 4.0 License.

Table 1. List of reactions with corresponding reaction rates (for three-body reactions [cm^6 $molecule^{-2}$ s^{-1}], for two-body reactions [cm^3 $molecule^{-1}$ s^{-1}]) taken from Burkholder et al. (2020).

	Reaction	Rate constant
R1	$O+O_2+M \rightarrow O_3+M$	$k_1 = 6.1 \cdot 10^{-34}(298/T)^{2.4}$
R2	$H+O_3 \rightarrow O_2+OH$	$k_2 = 1.4 \cdot 10^{-10} exp(-470/T)$
R3	$O+HO_2 \rightarrow O_2+OH$	$k_3 = 3 \cdot 10^{-11} exp(200/T)$
R4	$H+O_2+ M \rightarrow HO_2+M$	$k_4 = 5.3 \cdot 10^{-32}(298/T)^{1.8}$
R5	$H+HO_2 \rightarrow O_2+H_2$	$k_5 = 6.9 \cdot 10^{-12}$
R6	$H+HO_2 \rightarrow O+H_2O$	$k_6 = 1.6 \cdot 10^{-12}$

https://doi.org/10.5194/egusphere-2023-1046
Preprint. Discussion started: 5 June 2023
© Author(s) 2023. CC BY 4.0 License.

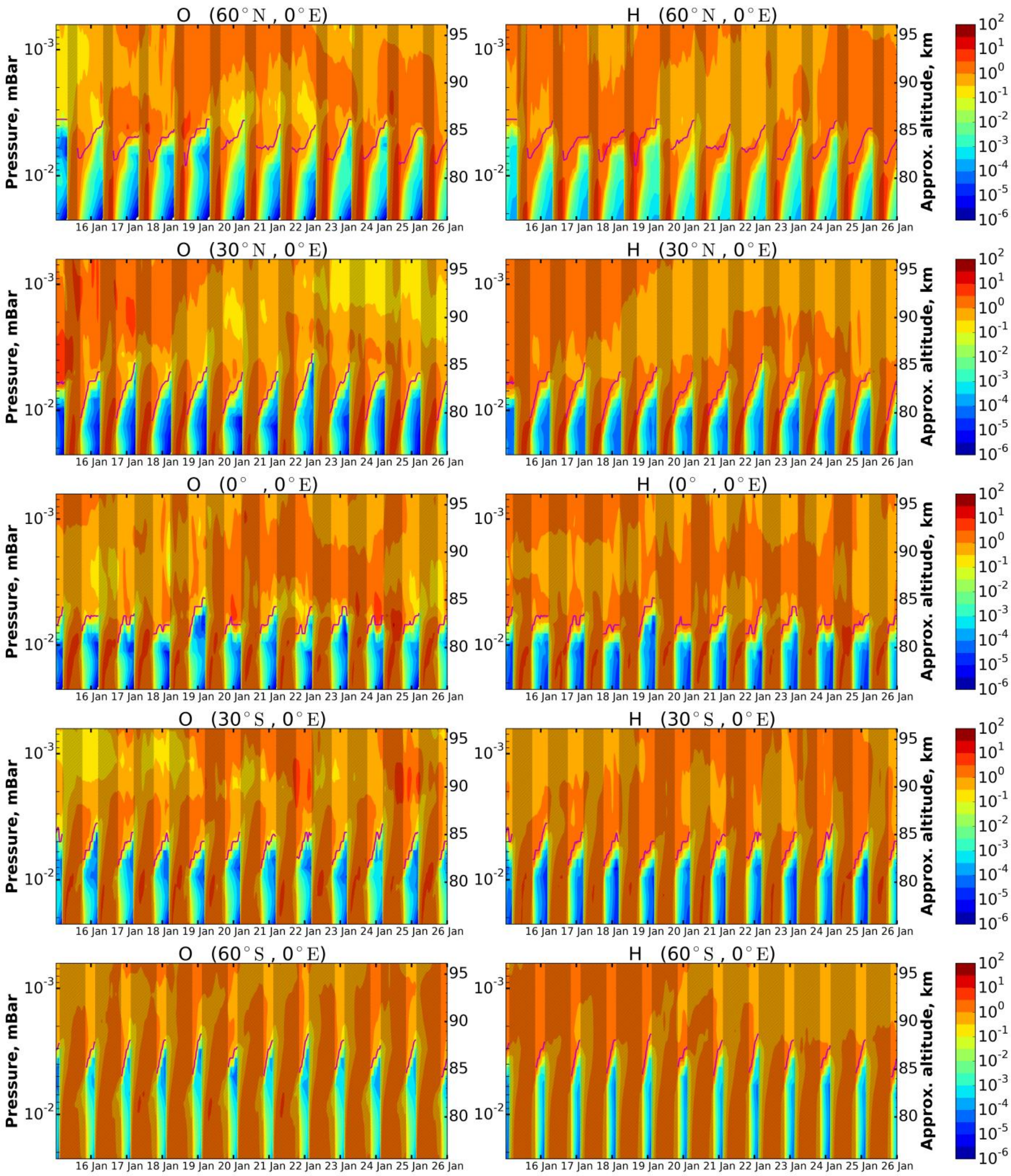

Figure 1. O and H time-height variations above different points in January calculated by the 3D chemical transport model of the middle atmosphere. The concentrations are normalized by mean daily values, correspondingly The dark bars mark daytime, light bars mark nighttime. The magenta lines point the NOCE boundary in accordance to criterion (5) (Cr = 0.1).

https://doi.org/10.5194/egusphere-2023-1046
Preprint. Discussion started: 5 June 2023
© Author(s) 2023. CC BY 4.0 License.

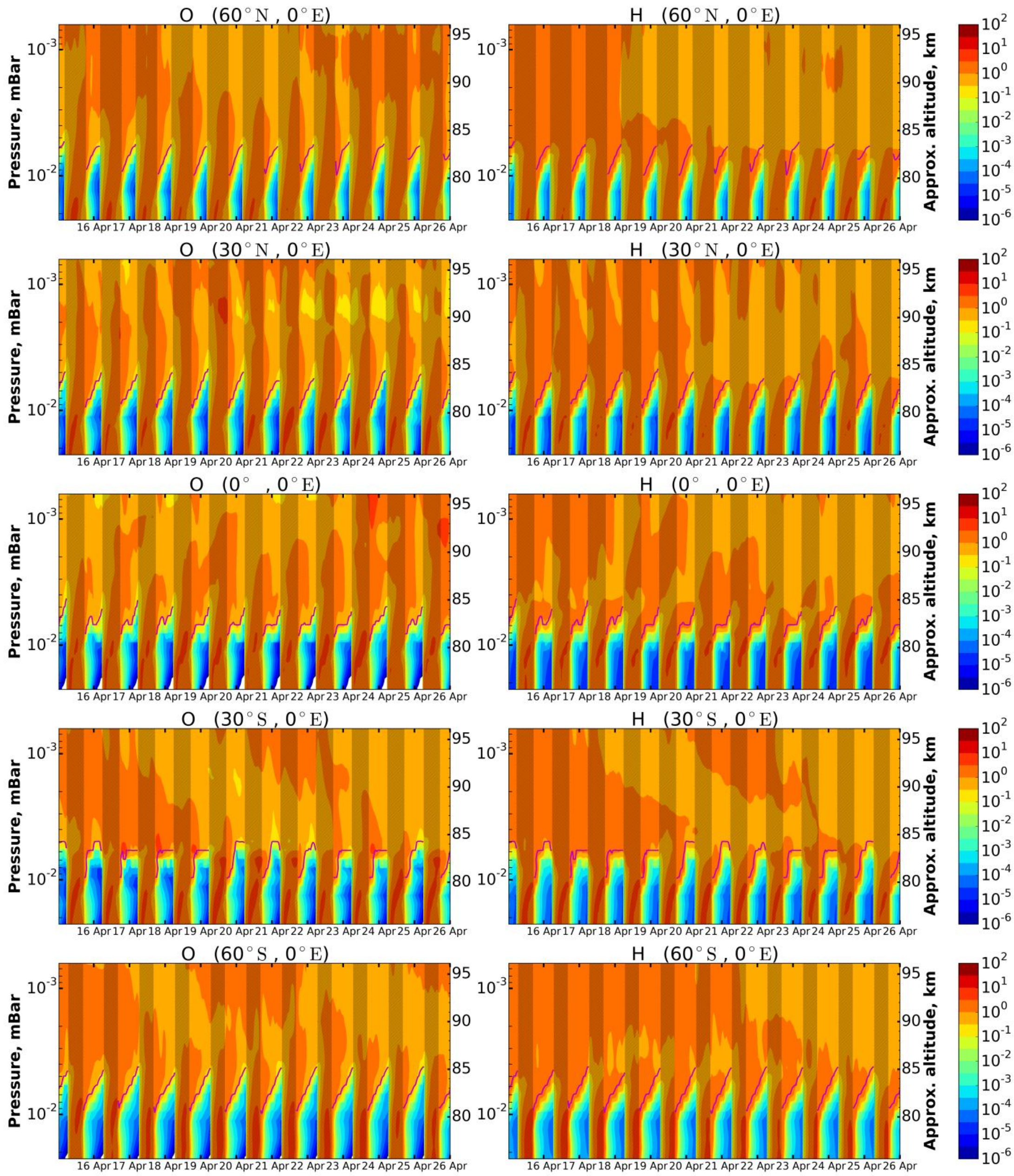

Figure 2. The same as in Fig. 1, but in April.

https://doi.org/10.5194/egusphere-2023-1046
Preprint. Discussion started: 5 June 2023
© Author(s) 2023. CC BY 4.0 License.

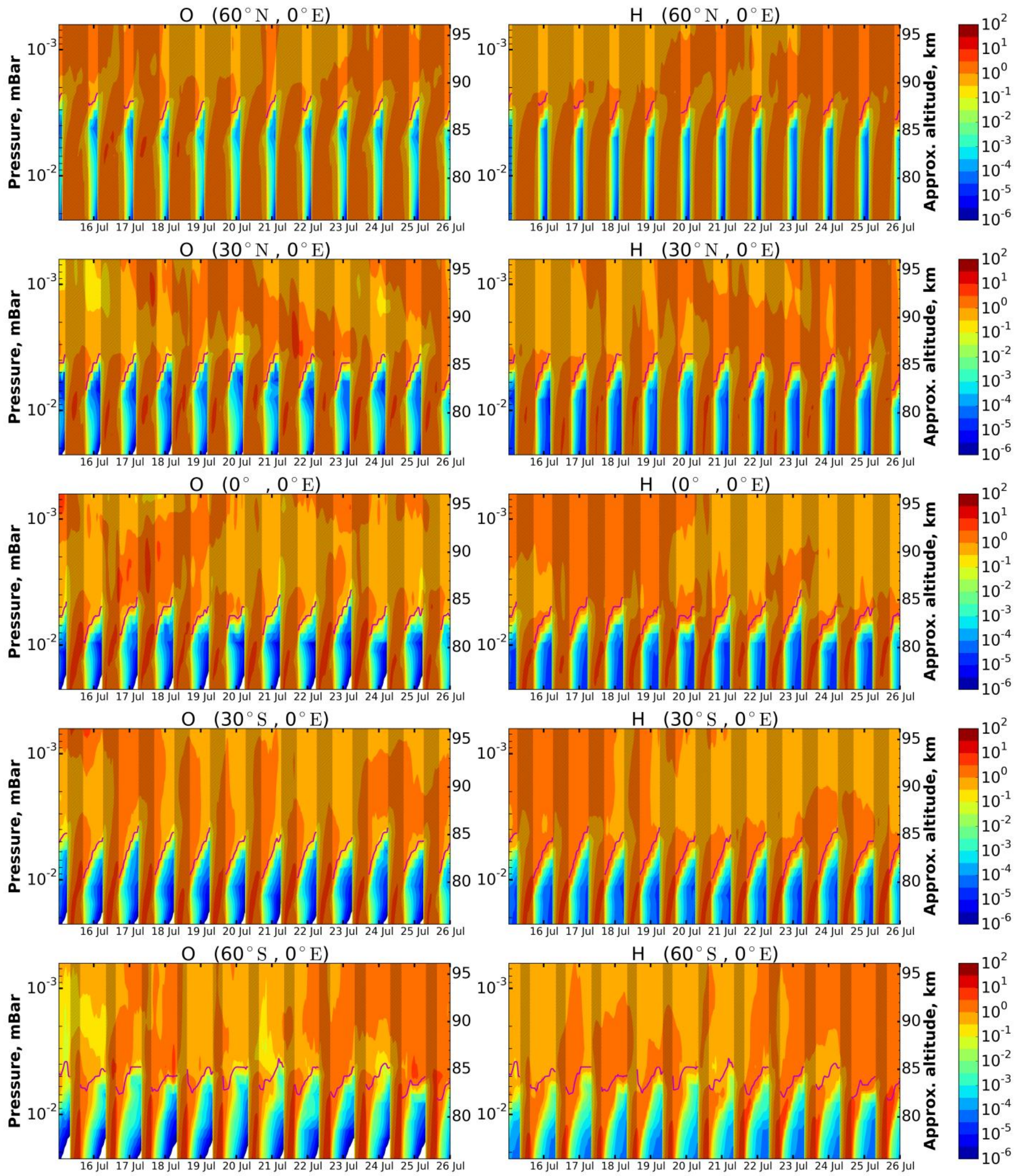

Figure 3. The same as in Fig. 1, but in July.

https://doi.org/10.5194/egusphere-2023-1046
Preprint. Discussion started: 5 June 2023
© Author(s) 2023. CC BY 4.0 License.

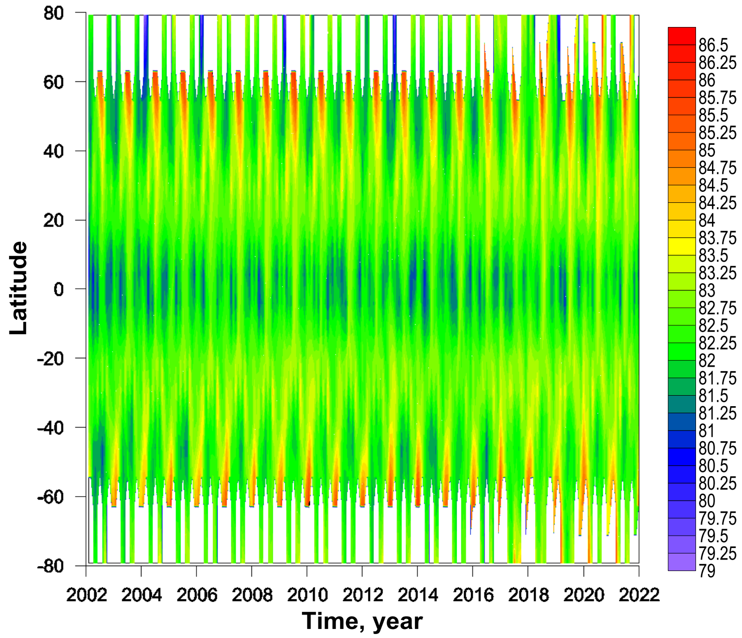

Figure 4. The space-time evolution of ${z_{eq}}^{pa}$. White color indicates data gaps due to the satellite sensing geometry.

https://doi.org/10.5194/egusphere-2023-1046
Preprint. Discussion started: 5 June 2023
© Author(s) 2023. CC BY 4.0 License.

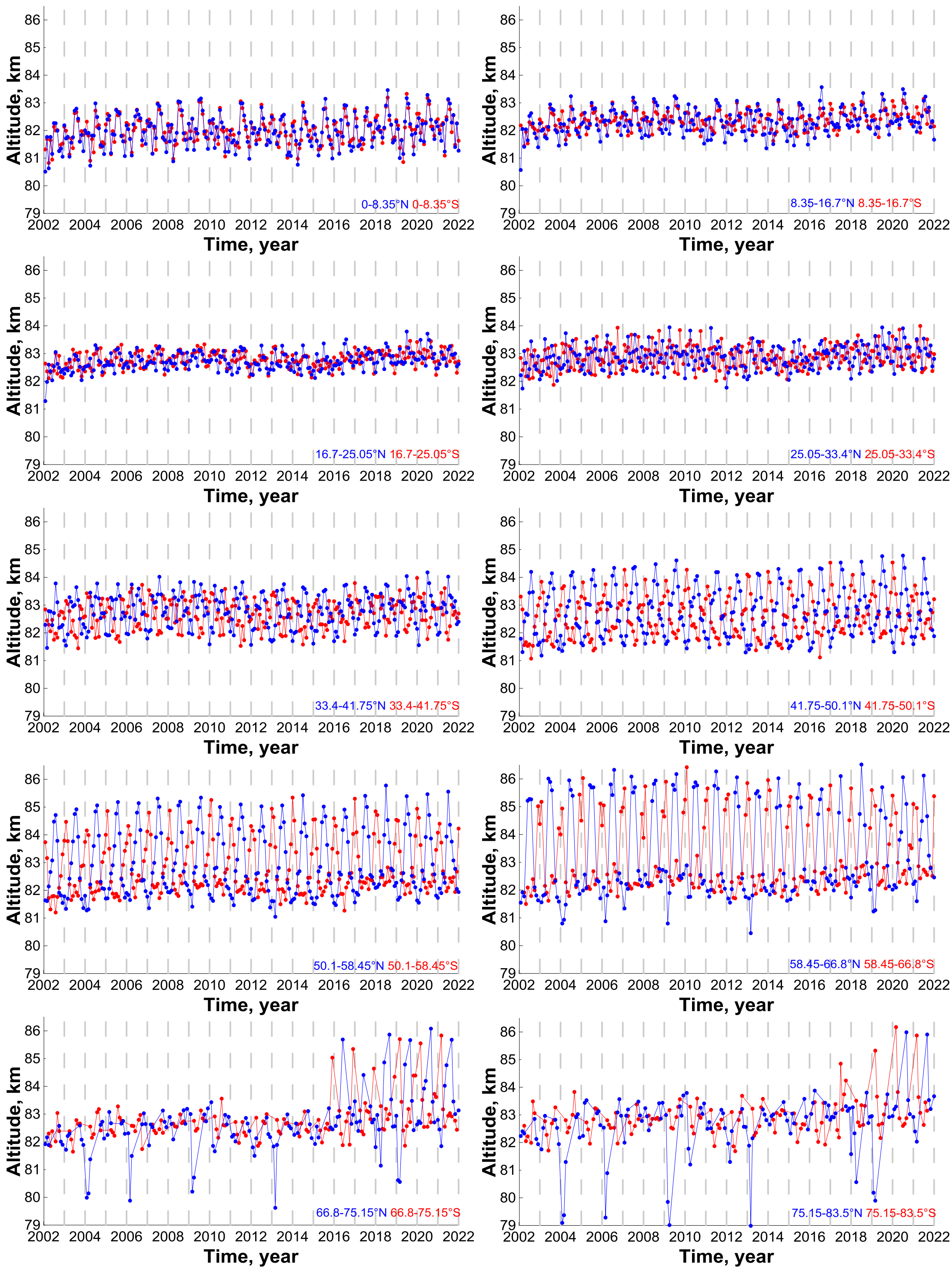

Figure 5. The time evolution of ${z_{eq}}^{pa}$ at different latitudes.

https://doi.org/10.5194/egusphere-2023-1046
Preprint. Discussion started: 5 June 2023
© Author(s) 2023. CC BY 4.0 License.

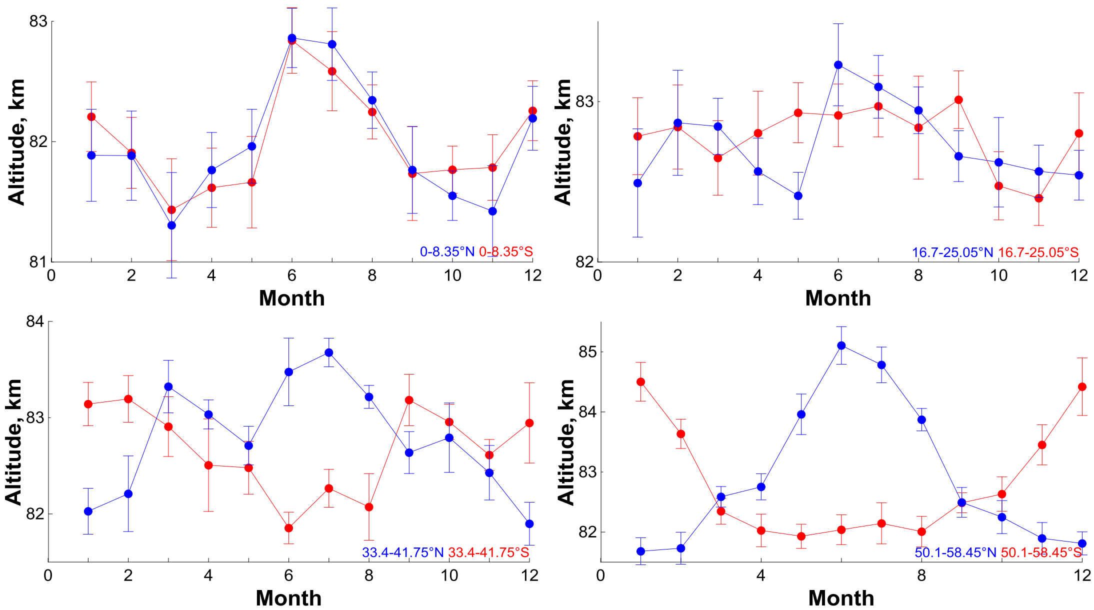

Figure 6. Average (for 2002-2021) annual cycle of ${z_{eq}}^{pa}$ at some latitudes.

https://doi.org/10.5194/egusphere-2023-1046
Preprint. Discussion started: 5 June 2023
© Author(s) 2023. CC BY 4.0 License.

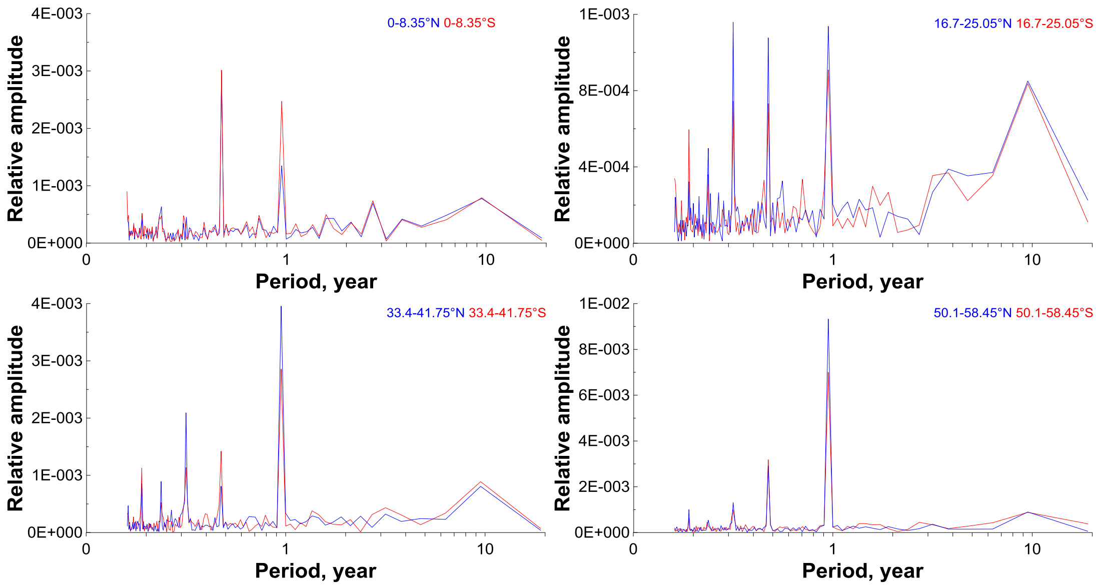

Figure 7. Fourier' spectra of $z_{eq}{}^{pa}$ time evolution at the same latitudes as in Figure 6. In each spectrum, the amplitudes of harmonics were normalized to corresponding zero harmonic.

https://doi.org/10.5194/egusphere-2023-1046
Preprint. Discussion started: 5 June 2023
© Author(s) 2023. CC BY 4.0 License.

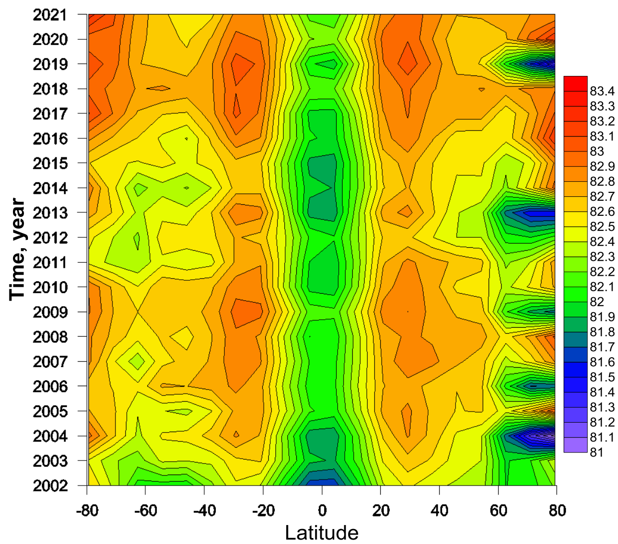

Figure 8. The latitude-time evolution of average annual $z_{eq}{}^{pa}$.

https://doi.org/10.5194/egusphere-2023-1046
Preprint. Discussion started: 5 June 2023
© Author(s) 2023. CC BY 4.0 License.

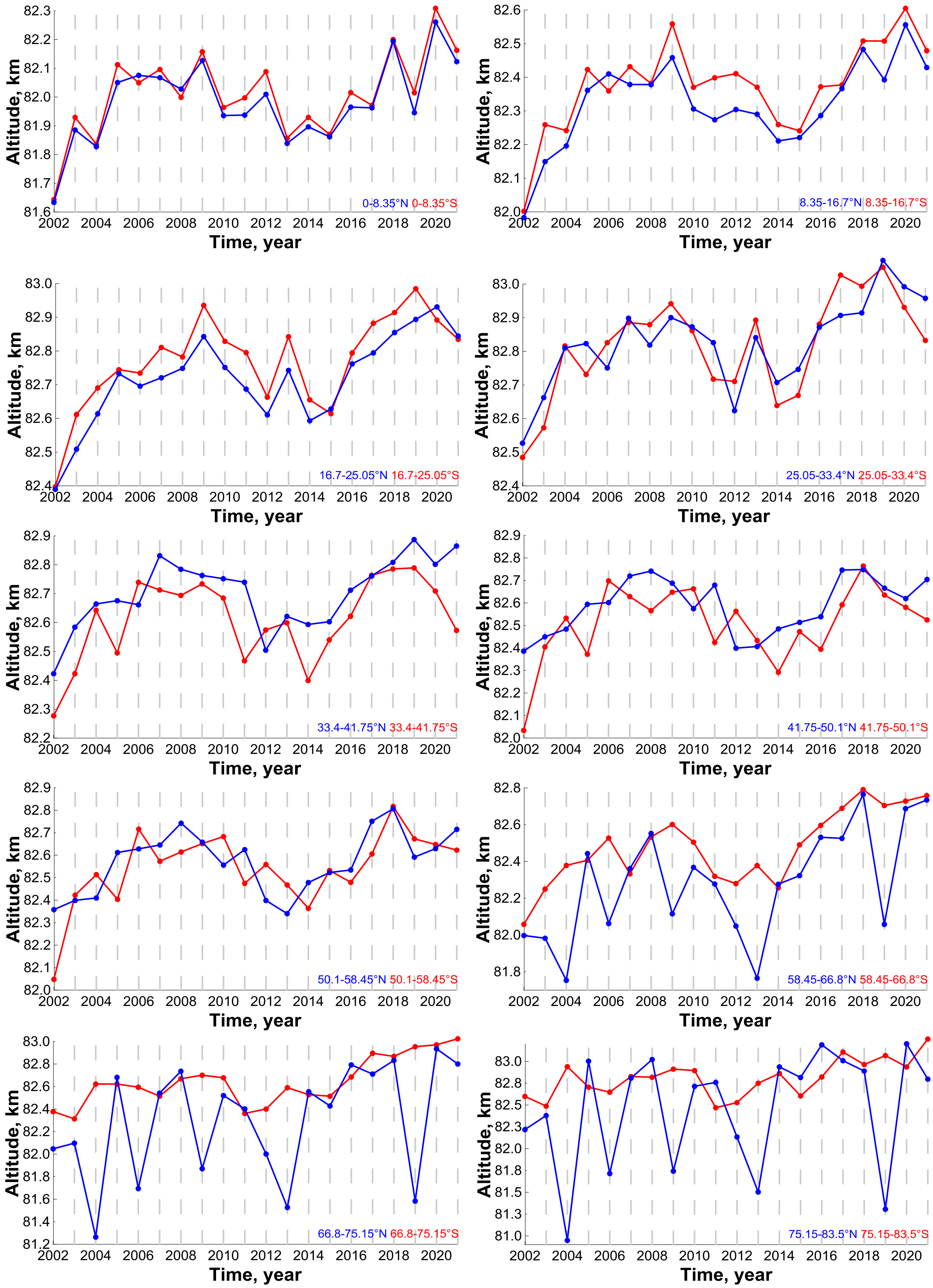

Figure 9. The time evolution of average annual $z_{eq}{}^{pa}$ ($< z_{eq}{}^{pa} >$) at different latitudes.

https://doi.org/10.5194/egusphere-2023-1046
Preprint. Discussion started: 5 June 2023
© Author(s) 2023. CC BY 4.0 License.

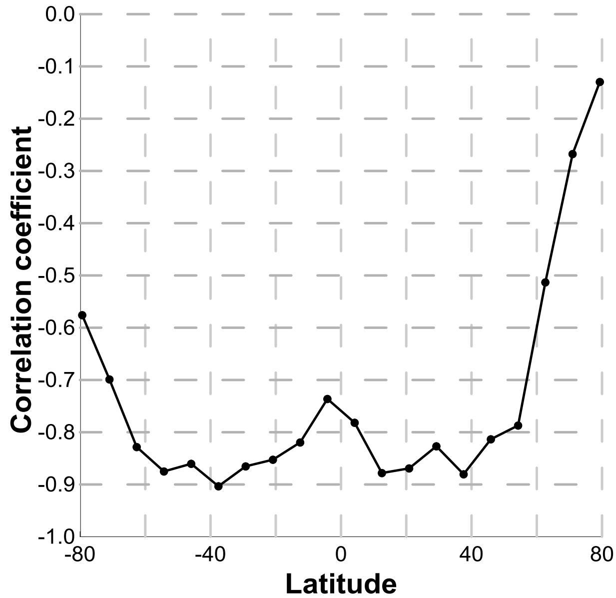

Figure 10. The correlation' coefficient of $< {z_{eq}}^{pa} >$ with $F_{10.7}$ index at different latitudes.

https://doi.org/10.5194/egusphere-2023-1046
Preprint. Discussion started: 5 June 2023
© Author(s) 2023. CC BY 4.0 License.

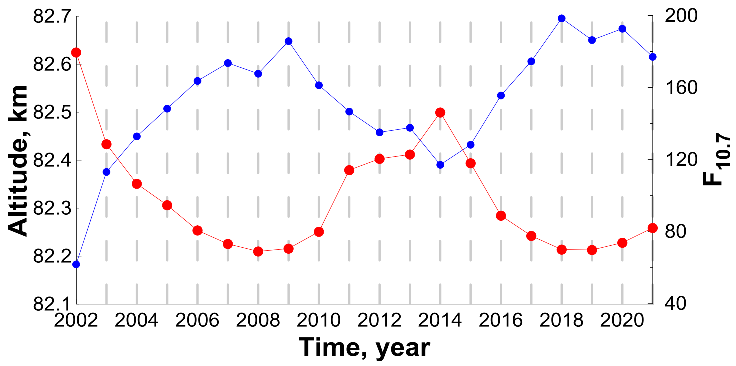

Figure 11. Red curve: $F_{10.7}$ index (solar radio flux at 10.7 cm). Blue curve: latitude-averaged $< {z_{eq}}^{pa} >$ in this range between ~55ºS and ~55ºN.

© Author(s) 2023. CC BY 4.0 License.

565

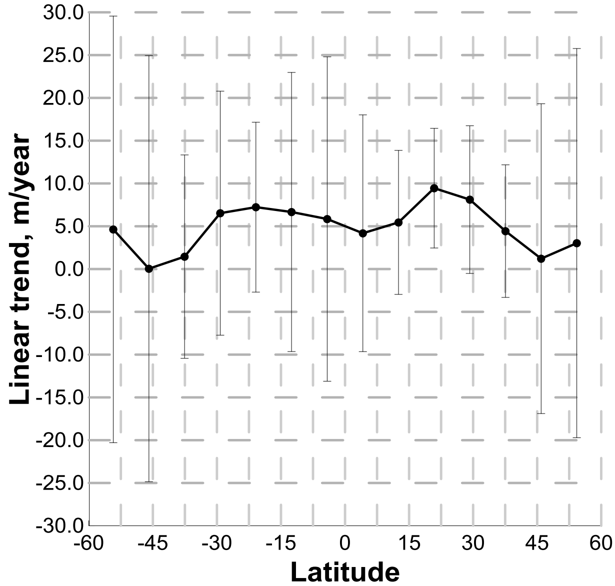

566

567 Figure 12. Linear trend in $< {z_{eq}}^{pa} >$ at different latitudes derived from multiregression analysis.

568

https://doi.org/10.5194/egusphere-2023-1046
Preprint. Discussion started: 5 June 2023
© Author(s) 2023. CC BY 4.0 License.

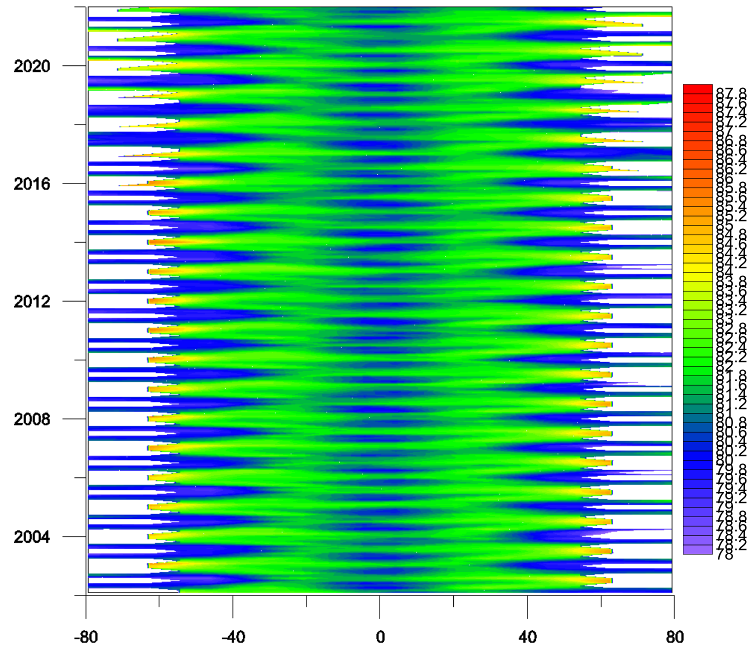

Figure 13. The space-time evolution of z_{eq}. White color indicates data gaps due to the satellite sensing geometry.

https://doi.org/10.5194/egusphere-2023-1046
Preprint. Discussion started: 5 June 2023
© Author(s) 2023. CC BY 4.0 License.

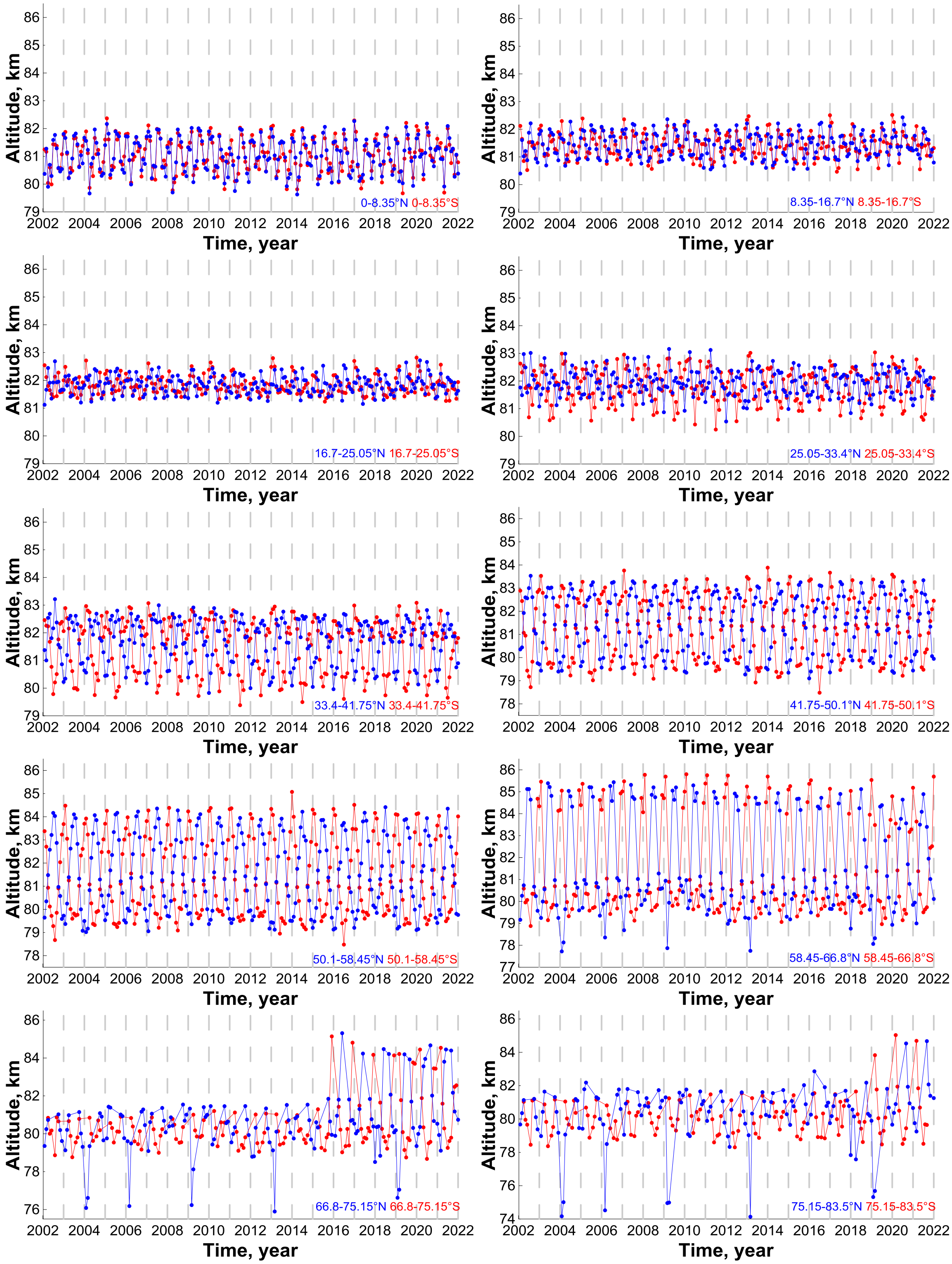

Figure 14. The time evolution of z_{eq} at different latitudes.

https://doi.org/10.5194/egusphere-2023-1046
Preprint. Discussion started: 5 June 2023
© Author(s) 2023. CC BY 4.0 License.

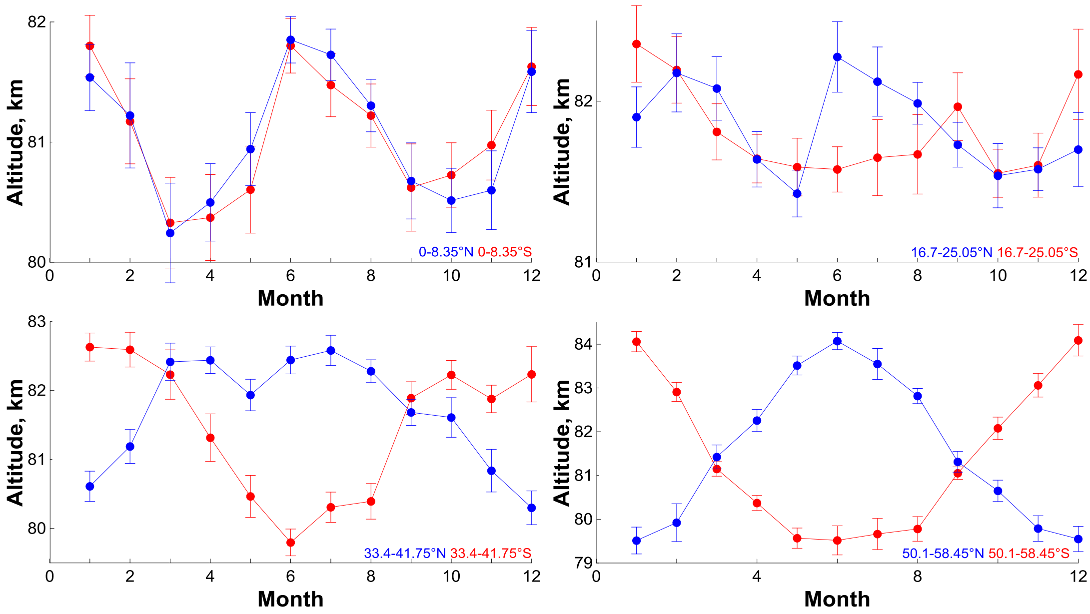

Figure 15. Average (for 2002-2021) annual cycle of z_{eq} at some latitudes.

https://doi.org/10.5194/egusphere-2023-1046
Preprint. Discussion started: 5 June 2023
© Author(s) 2023. CC BY 4.0 License.

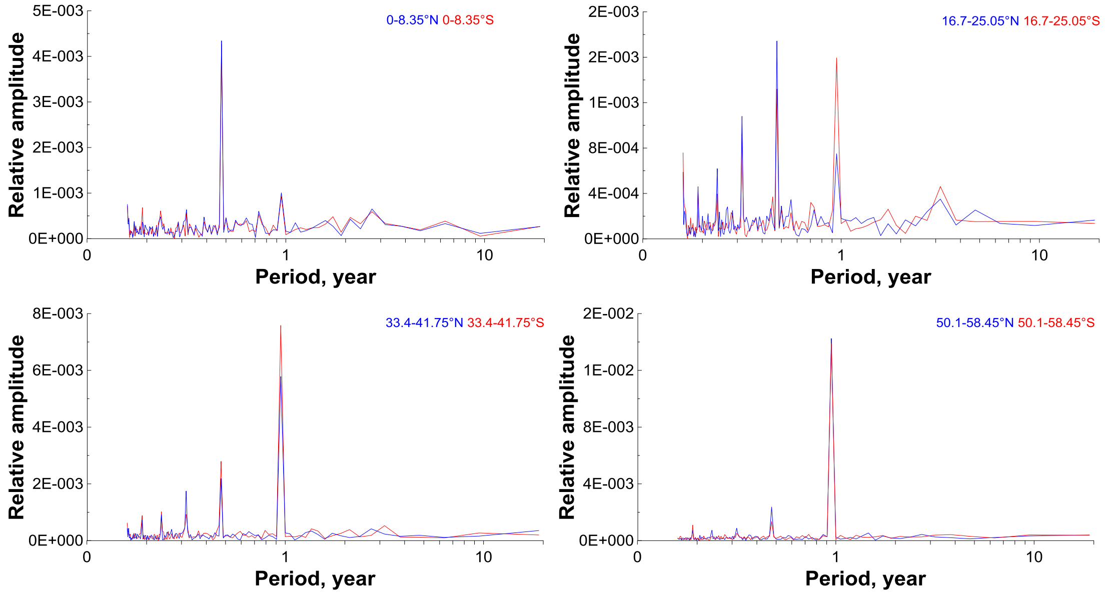

Figure 16. Fourier' spectra of z_{eq} time evolution at different latitudes. In each spectrum, the amplitudes of harmonics were normalized to corresponding zero harmonic.

https://doi.org/10.5194/egusphere-2023-1046
Preprint. Discussion started: 5 June 2023
© Author(s) 2023. CC BY 4.0 License.

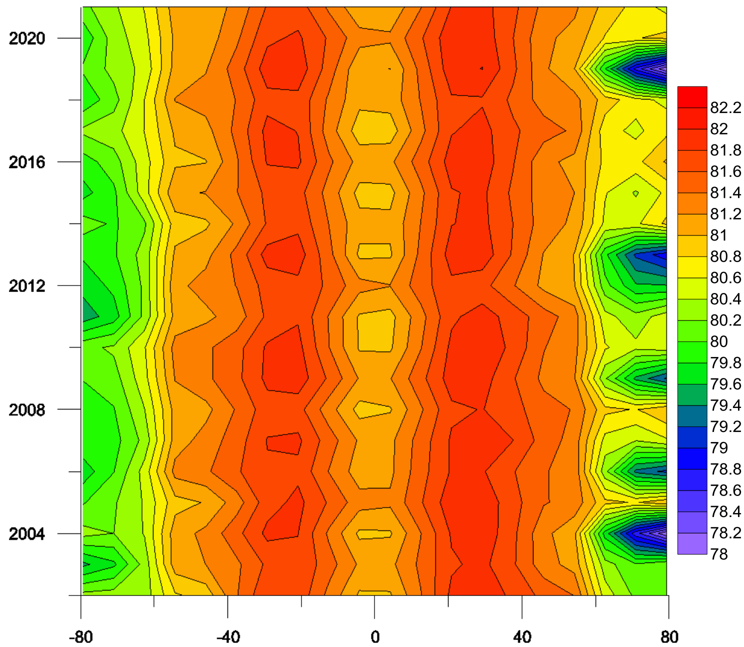

Figure 17. The latitude-time evolution of average annual z_{eq}.

https://doi.org/10.5194/egusphere-2023-1046
Preprint. Discussion started: 5 June 2023
© Author(s) 2023. CC BY 4.0 License.

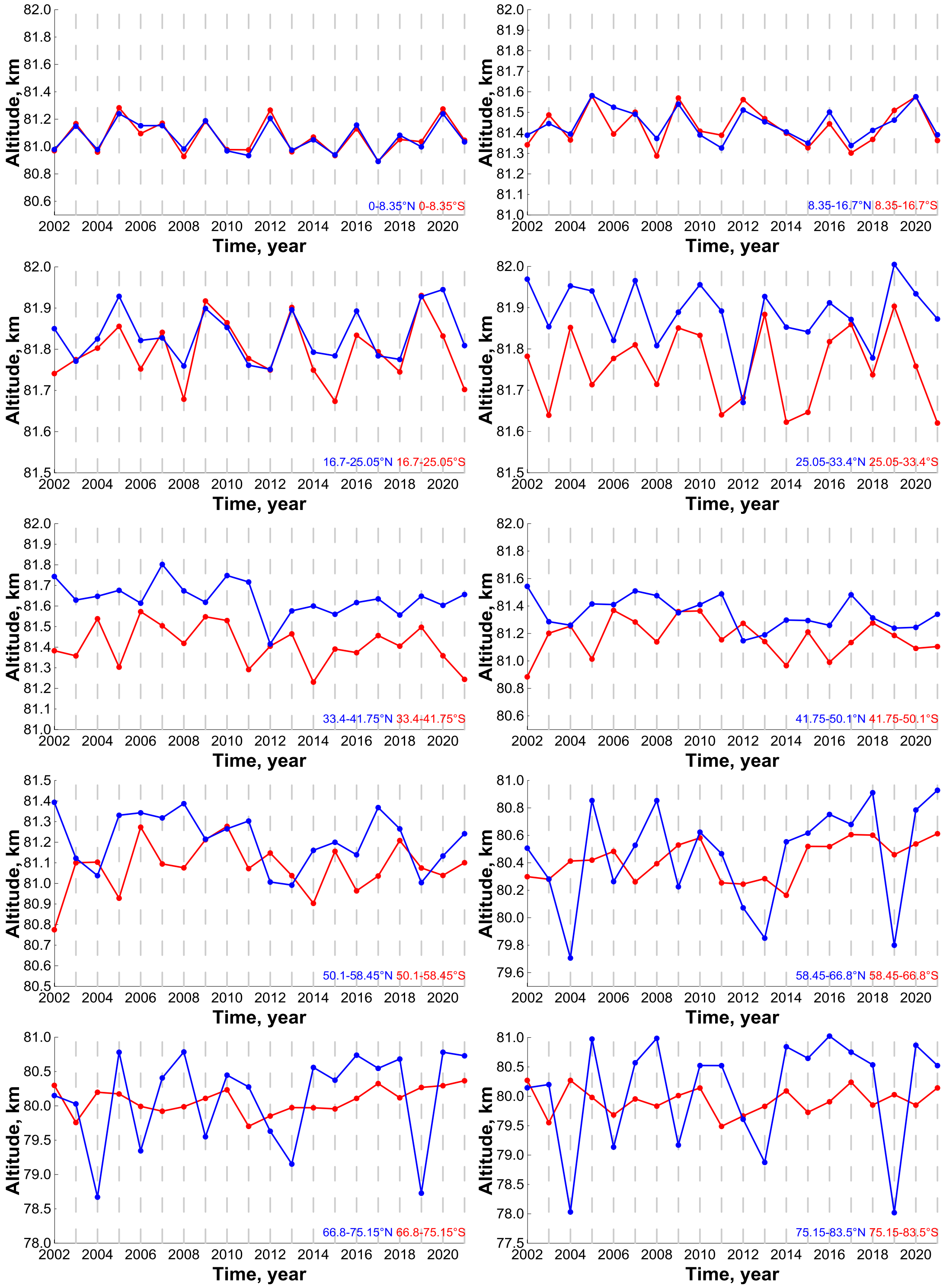

Figure 18. The time evolution of average annual z_{eq} ($< z_{eq} >$) at different latitudes.

https://doi.org/10.5194/egusphere-2023-1046
Preprint. Discussion started: 5 June 2023
© Author(s) 2023. CC BY 4.0 License.

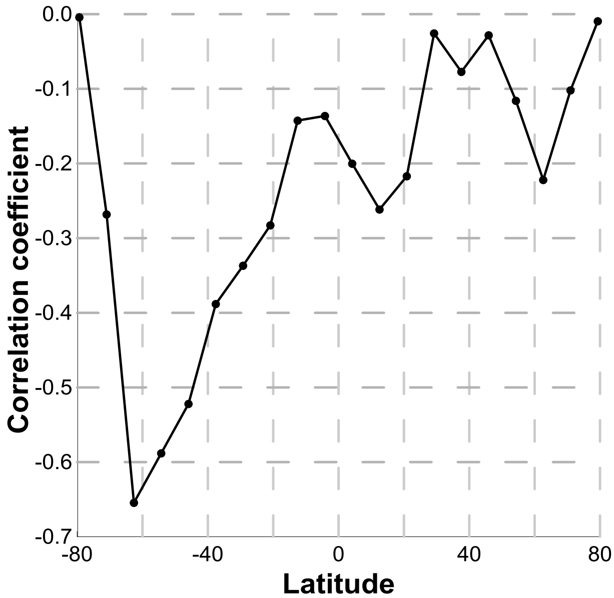

Figure 19. The correlation' coefficient of $< z_{eq} >$ with $F_{10.7}$ index at different latitudes.

https://doi.org/10.5194/egusphere-2023-1046
Preprint. Discussion started: 5 June 2023
© Author(s) 2023. CC BY 4.0 License.

602

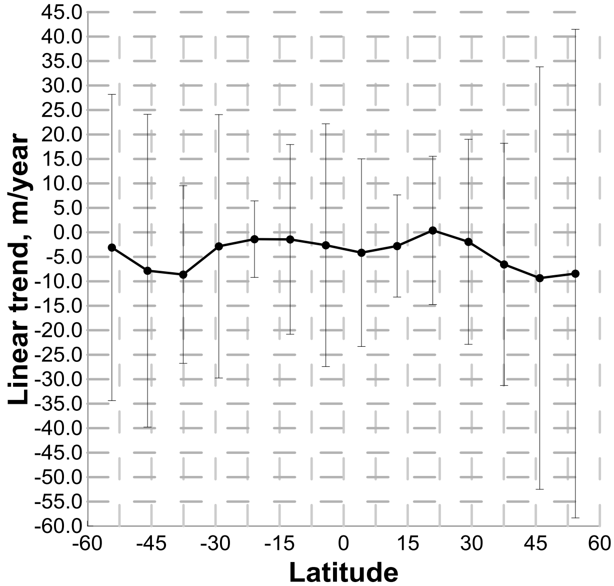

603

604 Figure 20. Linear trend in $< z_{eq} >$ at different latitudes derived from multiregression analysis.

605